ROYAL SOCIETY
OF CHEMISTRY

PAPER
Wen-Xiu Ni, Wai-Lun Man *et al.*
Cytotoxic *cis*-ruthenium(III) bis(amidine) complexes

Dalton Transactions

PAPER

Cytotoxic *cis*-ruthenium(III) bis(amidine) complexes†

Tao Liu,[a] Chen Pan,[a] Huatian Shi,[b] Tao Huang,[a] Yong-Liang Huang, [ID][a] Yang-Yang Deng,[a] Wen-Xiu Ni [ID] *[a] and Wai-Lun Man [ID] *[b]

In chemotherapy, the search for ruthenium compounds as alternatives to platinum compounds is proposed because of their unique properties. However, the geometry effect of ruthenium complexes is sparely investigated. In this paper, we report the synthesis of a series of bis(acetylacetonato)ruthenium(III) complexes bearing two amidines (1–) in a *cis* configuration. These complexes are highly cytotoxic against various cancer cell lines, including a cisplatin-resistant cell line. *In vitro* studies suggested that the representative complex can induce cell cycle G0/G1 phase arrest, decrease the mitochondrial membrane potential, elevate the intracellular reactive oxygen species level, and cause DNA damage and caspase-mediated mitochondrial pathway apoptosis in NCI-H460 cells. *In vivo*, it can effectively inhibit tumor xenograft growth in nude mouse models with no body weight loss. In combination with the reported *trans*-bis(amidine)ruthenium(III) complexes, we found that ruthenium(III) bis(amidine) complexes could be cytotoxic in both *trans* and *cis* geometries, which is in contrast to platinum-based compounds.

Introduction

In chemotherapy, the undesired side effects and acquired resistance to platinum-based compounds have motivated the search for other metal-based anticancer agents.[1–3] Ruthenium complexes are the best alternative with unique properties, including a good binding ability to biological molecules, low toxicity, and high selectivity.[4,5] So far, many ruthenium-based anticancer agents have been reported with promising *in vitro* and *in vivo* activities; they are well-designed with precious ancillary ligands that could be systematically tuned with steric and electronic effects.[6–9] Surprisingly, the geometry effect of these ruthenium complexes is less explored. For example, Glazer *et al.* reported the biological properties of the polypyridyl ruthenium(II) diamine complex.[10] To the tested HL-60 and A549 cell lines, the *trans* isomer is cytotoxic, while its *cis* analog is intrinsically inactive (Fig. 1). This result contrasts with the well-known platinum-based anticancer drugs, of which cisplatin is highly active, but transplatin is ineffective in cancer treatment.

Inspired by the recent work reported by Zhu *et al.*, the axial ligands on (salen)ruthenium(III) complexes have shown a profound effect on the mechanism of killing cancer cells. In the *trans*-configuration, the two amidine ligands coordinated to the planar (salen)ruthenium(III) complexes can induce cancer cell death *via* the *para*-apoptosis mechanism.[11] These bis(amidine) complexes are easily accessed by nucleophilic attack of appropriate amines to the acetonitrile coordinated onto the ruthenium(III) center. In this work, we prepared the complex *cis*-[Ru^{III}(acac)$_2$(NCCH$_3$)$_2$]$^+$ [acac = acetylacetonate(1–)] and synthesized a series of bis(amidine)ruthenium(III) complexes in the *cis*-configuration. These complexes are highly active toward the tested cancer cell lines. The possible anti-cancer mecha-
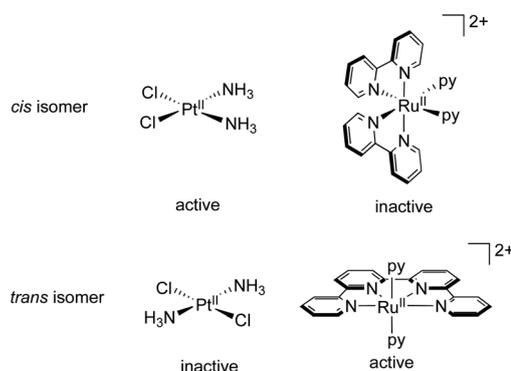
[a]Department of Medicinal Chemistry, Shantou University Medical College, Shantou, Guangdong, 515041, P.R. China. E-mail: wxni@stu.edu.hk

[b]Department of Chemistry, Hong Kong Baptist University, Kowloon Tong, Hong Kong, P.R. China. E-mail: wlman118@hkbu.edu.hk

†Electronic supplementary information (ESI) available. CCDC 2223820. For ESI and crystallographic data in CIF or other electronic format see DOI: https://doi.org/10.1039/d3dt00328k

Fig. 1 The drawings of the *cis/trans*-isomers of (polypyridyl)ruthenium(II) and diamminedichloroplatinum(II).

nisms, which included colony formation, cell cycle arrest, induction of apoptosis, mitochondrial membrane potential (MMP) change, reactive oxygen species (ROS) elevation, and the protein expression level, were explored using various methods. Moreover, the *in vivo* antitumor potency of the representative complex was evaluated using a xenograft mouse model.

Fig. 2 The structures of **1–6**.

Results and discussion

Synthesis and characterization

The amidine complexes can be readily accessed by nucleophilic attack of the amines onto the nitriles coordinated to the ruthenium(III) ion (Scheme 1). The purple complex *cis*-[$Ru^{III}(acac)_2(NCCH_3)_2$]$^+$ was prepared according to the literature method.[12] Treatment of $Ru^{III}(acac)_3$ with 1.2 equiv. of HX (X = ClO_4^- or $CF_3SO_3^-$) in CH_3CN at room temperature afforded the corresponding compound *cis*-[$Ru^{III}(acac)_2(NCCH_3)_2$](X) in high yield. These compounds were used without further purification. Addition of 10 equiv. of primary amines (RNH_2) to *cis*-[$Ru^{III}(acac)_2(NCCH_3)_2$]$^+$ in CH_3CN at room temperature afforded a deep red solution in 10 min. After evaporation of the volatiles and recrystallization from CH_3CN/Et_2O, a series of *cis*-ruthenium(III) bis(amidine) complexes, with the general formula of *cis*-[$Ru^{III}(acac)_2(NH=C(CH_3)NHR]^+$ (**1–6**), were isolated (Fig. 2).

Mass spectrometry shows the dominant peaks corresponding to their parent ions. Fig. 3A shows the representative ESI-MS of complex **6**. The dominant peak at a mass-to-charge ratio (m/z) of 584 is assigned to the parent ion with the formula [$Ru(acac)_2(NH=C(CH_3)NH(CH_2)_5CH_3)_2$]$^+$. This assignment is supported by the excellent agreement between the experimental and simulated patterns of the peak (insets). The MALDI-TOF mass spectra (positive mode) of other complexes are shown in Fig. S1–S5.†

We have also done the cyclic voltammetry (CV) of complexes **5** and **6** in CH_3CN using 0.1 M [N^nBu_4](PF_6) as the supporting electrolyte. All potentials are reported in volts (V) with refer-
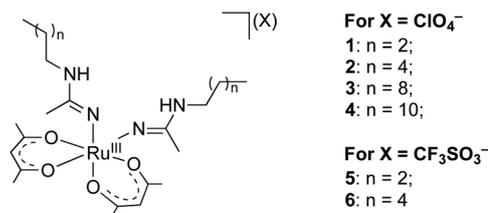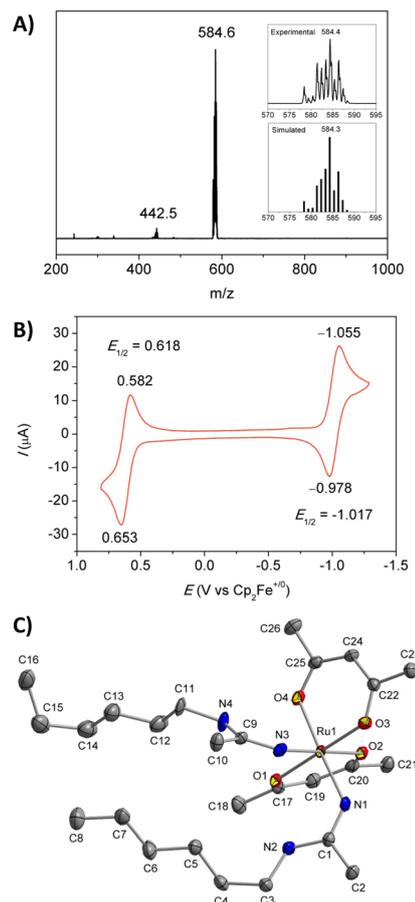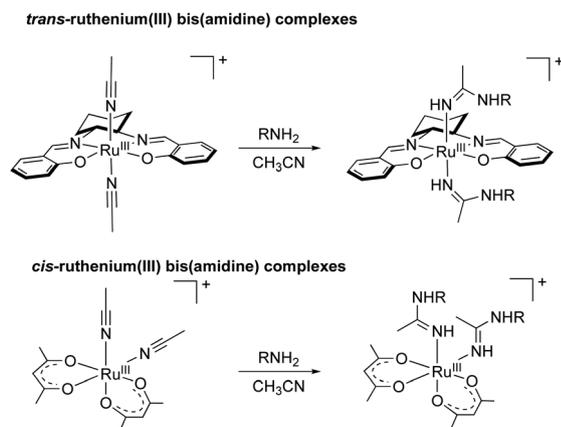

Fig. 3 Characterization of **6(CF₃SO₃)**. (A) ESI mass spectrum (positive mode) in CH_3CN. Insets show the peak's experimental (top) and simulated (bottom) patterns. (B) CV in CH_3CN. (C) X-ray structure of the cation. The solvent molecule and hydrogen atoms are omitted for clarity.

Scheme 1 The synthesis of *trans*- and *cis*-ruthenium(III) bis(amidine) complexes.

ence to ferrocenium/ferrocene ($Cp_2Fe^{+/0}$). In Fig. 3B, the two reversible couples at +0.62 V (ΔE_p = 71 mV) and −1.02 V (ΔE_p = 77 mV) are assigned to the metal-centered $Ru^{IV/III}$ and $Ru^{III/II}$ couples of **6**, respectively. The reduction potentials of both $Ru^{IV/III}$ and $Ru^{III/II}$ couples are insensitive to the length of the alkyl chain. In complex **5**, these couples occurred at $E_{1/2}$ = +0.62 and −1.01 V (Fig. S6†). Both complexes **5** and **6** are stable in CH_3CN in air, similar to the *trans*-[$Ru^{III}(salen)(NH=C(CH_3)NH(CH_2)_5CH_3)_2$]$^+$ with an $E_{1/2}$ of $Ru^{IV/III}$ and $Ru^{III/II}$ = +0.36 and −1.13 V respectively in CH_3CN.

The molecular structure of complex **6** has been determined by X-ray crystallography (Fig. 3C and Tables S1–S2†). The structure clearly shows that two amidines are bonded to the ruthenium center, *cis* to each other. The bond distances of Ru(1)–N (1) and Ru(1)–N(3) are 2.034(3) Å and 2.038(4) Å, respectively, which are slightly shorter (Ru–$N_{amidine}$ = 2.070(3) Å) than that in *trans*-[Ru^{III}(salen)(NH=C(CH$_3$)NH(CH$_2$)$_5$CH$_3$)$_2$]$^+$.

Stability

UV-vis spectroscopy was used to investigate the stability of **1–6** in various solvents (Fig. S7 and S8†). All complexes are stable in neat DMSO at room temperature with no notable spectral changes for 24 h. They are also stable (except for **3** and **4**) in phosphate-buffered saline (PBS, with 1% DMSO) solution. The decline of the UV-vis spectra of **3** and **4** in the PBS solution was presumably due to the decreasing solubility in the aqueous solution when the alkyl chain length increased in the amidine moiety. Notable precipitates were observed after standing the PBS solutions of **3** and **4** for 24 h.

Cytotoxicity

MTT assay ([3-(4,5-dimethylthiazol-2-yl)-2,5-diphenyltetrazolium bromide]) evaluated the *in vitro* cytotoxicity of complexes **1–6** against a panel of human cancer cell lines, including liver hepatocellular (HepG2), cervical epithelioid (HeLa), breast (MCF-7), ovarian (A2780), and lung (NCI-H460, A549, A549/DDP). IC$_{50}$ values are summarized in Table 1. The IC$_{50}$ value is the dose required to inhibit 50% cellular growth for 48 h. Cisplatin (used as a positive control) exhibits micromolar IC$_{50}$ values toward the tested cancer cell lines (except for A549/DPP), which aligned with the results found in other research groups. Generally, **1–6** exhibit similar or slightly higher cytotoxicity than cisplatin. The cytotoxicity of these complexes varies with the length of the alkyl chain. Increasing the number of CH$_2$ groups in the amidine moieties decreases the IC$_{50}$ value and reaches the minimum when n = 8 (complex **3**, Fig. 2). However, further increasing the chain length to n = 10 (complex **4**) lowers the cytotoxicity. On the other hand, the cytotoxicity of these ruthenium(III) complexes is insensitive to the counterions. The IC$_{50}$ values are the same for the ClO$_4^-$ or CF$_3$SO$_3^-$ complexes. It is known that cisplatin is less cytotoxic

to the cisplatin-resistant cell line (A549/DDP). A large resistance factor (RF) value of 14.4 is observed. RF value is defined as IC$_{50}$ in (A549/DDP)/IC$_{50}$ in A549. In contrast, complexes **1–6** are highly active toward the A549/DDP cell line, with low RF values ranging from 0.8 to 1.2. This result suggested that complexes **1–6** are potential drugs to overcome the resistance to platinum-based anticancer drugs. Considering the stability, solubility, and cytotoxicity, we have selected complex **6** as the representative candidate for further *in vitro* and *in vivo* studies using NCI-H460 cells. Apart from the MTT assay, the colony formation assay is a well-established method to evaluate the antiproliferative activity of anticancer agents.[13] Fig. 4A shows the dose-dependent suppression of colony formation in **6**-treated NCI-H460 cells. For the NCI-H460 cells treated with 0.5 μM **6**, 75% of colonies were observed. When the concentration of **6** was increased to 1, 2, and 4 μM, the colonies significantly dropped to 55, 8, and 2%, respectively. No colony formation was observed for the NCI-H460 cells when treated with 8 μM **6**. This result agrees with the IC$_{50}$ value adapted in the above MTT assay. We have also performed the EdU incorporation assay to examine the rate of DNA replication. EdU (5-ethynyl-2′-deoxyuridine) can substitute thymidine by incorporating newly synthesized DNA during DNA synthesis. The proportion of EdU-positive cells significantly decreased dose-dependently after treatment with complex **6** (Fig. 4B).

Cell cycle progression

Cell proliferation inhibition by hindering cell cycle progression is known to many anticancer agents.[14] Hence, we have investigated the cell cycle distribution of **6**-treated NCI-H460 cells by flow cytometry using propidium iodide (PI) staining (Fig. 5A). The G0/G1 phase population of the untreated group was 43.0%. After treatment with 8 μM complex **6**, the G0/G1 phase population increased to 52.3 and 61.6% at 12 and 24 h, respectively, indicating a G0/G1 phase arrest. Furthermore, a concentration-dependent G0/G1 phase arrest was also found in **6**-treated cells (Fig. S9†). To further elucidate **6**-induced cell cycle arrest, we examined the level of proteins in cell cycle distribution by western blotting. The transcription factor E2F-1 plays a vital role in the G1/S transition of cell cycle progression. Retinoblastoma protein (Rb) is a typical tumoral suppressor

---

Table 1 Cytotoxicity of *cis*-ruthenium(III) bis(amidine) complexes **1–6**

| Compound | IC$_{50}$^{a} (μM) | | | | | | | RF^b |
	HepG2	HeLa	MCF-7	A2780	NCI-H460	A549	A549/DDP	
1	11.0 ± 2.4	1.82 ± 0.92	1.32 ± 0.13	2.09 ± 1.01	1.83 ± 0.07	2.40 ± 0.40	1.88 ± 0.42	0.8
2	2.66 ± 0.36	1.15 ± 0.52	0.83 ± 0.27	0.55 ± 0.10	0.92 ± 0.06	1.62 ± 0.28	1.25 ± 0.16	0.8
3	0.85 ± 0.18	0.19 ± 0.01	0.24 ± 0.06	0.23 ± 0.01	0.18 ± 0.01	0.22 ± 0.05	0.27 ± 0.01	1.2
4	4.30 ± 0.35	1.85 ± 0.41	2.67 ± 0.48	2.24 ± 0.48	2.13 ± 0.28	2.30 ± 0.52	1.97 ± 0.18	0.8
5	13.5 ± 1.77	1.87 ± 0.46	1.58 ± 0.07	1.78 ± 0.45	1.63 ± 0.19	1.76 ± 0.36	1.81 ± 0.49	1.0
6	3.00 ± 0.85	0.64 ± 0.02	0.51 ± 0.01	0.72 ± 0.01	0.77 ± 0.02	0.71 ± 0.01	0.66 ± 0.07	0.9
Cisplatin	3.58 ± 0.72	5.12 ± 0.22	4.24 ± 0.40	11.6 ± 0.04	3.02 ± 0.03	10.6 ± 0.71	153.8 ± 5.0	14.4

^{a} 50% inhibitory concentration after exposure for 48 h in the MTT assay. ^{b} Resistance factor calculated from the ratio of IC$_{50}$(A549/DPP) to IC$_{50}$(A549).
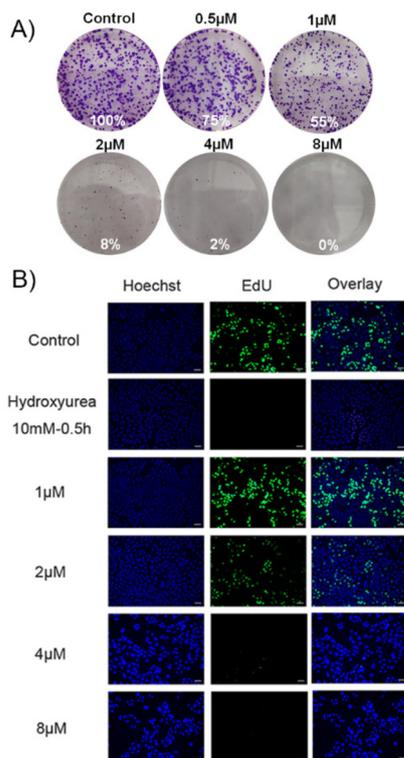
Fig. 4 (A) Inhibitory effect of **6** on colony formation in NCI-H460 cells. (B) NCI-H460 cell proliferation determined by EdU staining. Typical images of EdU-stained proliferating cell nuclei (green) and Hoechst-stained cell nuclei (blue) and merged images are shown (scale bar: 100 mm).
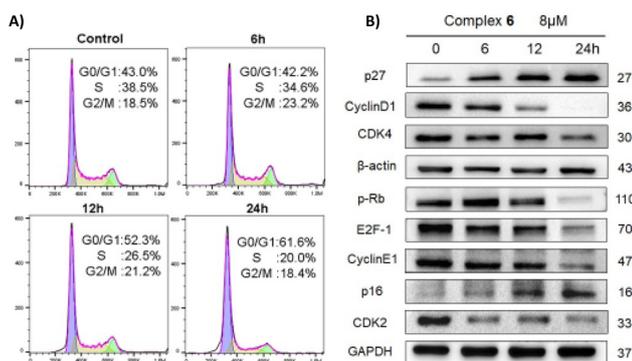

Fig. 5 (A) NCI-H460 cell cycle distribution for 0–24 h after treatment with **6** (8 μM) as determined by flow cytometry. (B) Protein expression levels of **6**-treated (8 μM) NCI-H460 cells assessed by western blotting.

which can be hyper-phosphorylated to its inactivated form by cyclins and CDKs, such as CyclinD1-CDK4/6 and CyclinE-CDK2 and allow E2F-1 releases. CDKs can be inhibited by specific cyclin-dependent kinase inhibitors (CKIs) such as p27 and p16, resulting in G1 phase arrest.[15–17] As clearly shown in Fig. 5B and Fig. S10,† complex **6** suppressed the levels of relevant cell cycle regulatory proteins, including CDK2, CDK4, CyclinE1, CyclinD1, p-Rb, and E2F-1. At the

same time, it significantly uplifted the levels of p27 and p16 in NCI-H460 cells. These results indicated that **6** could induce G0/G1 phase cell cycle arrest in both time- and dose-dependent manners.

Cell death pathway

Calcein-AM/PI double staining assay was conducted to distinguish between the live cells (green fluorescence) and dead cells (red fluorescence). As shown in Fig. 6, the number of dead cells increased significantly after treatment with different concentrations of complex **6**. To understand the cell death mechanism, we initially investigated whether complex **6** induced cell apoptosis in NCI-H460 cells by flow cytometry. Annexin V-FITC/PI double staining cells are shown in the flow chart, which contains four typical quadrants including normal cells (lower left quadrant), necrotic cells (upper left quadrant), early apoptotic cells (lower right quadrant), and late apoptotic cells (upper right quadrant). Compared with the control cells, the low dose of **6** (1 μM) resulted in insignificant apoptotic cells (early and late stage) of only 2.7%. When the concentration of **6** was increased to 8 and 10 μM, the apoptotic cells were uplifted to 28.4 and 51.5%, respectively (Fig. 7). In addition, the apoptotic rate was also increased from 16.4% (12 h) to 56.5% (48 h) when treated with 8 μM complex **6** (Fig. S11†).

Intracellular ROS detection

Intracellular reactive oxygen species (ROS) oxidative stress can induce cell apoptosis.[18,19] We determined the ROS levels in **6**-treated cells by inverted fluorescence microscopy and flow cytometry after staining with 2′,7′-dichlorodihydrofluorescein diacetate (DCFH-DA). In the presence of cellular ROS, DCFH-DA can be converted to DCF, which displays green fluo-
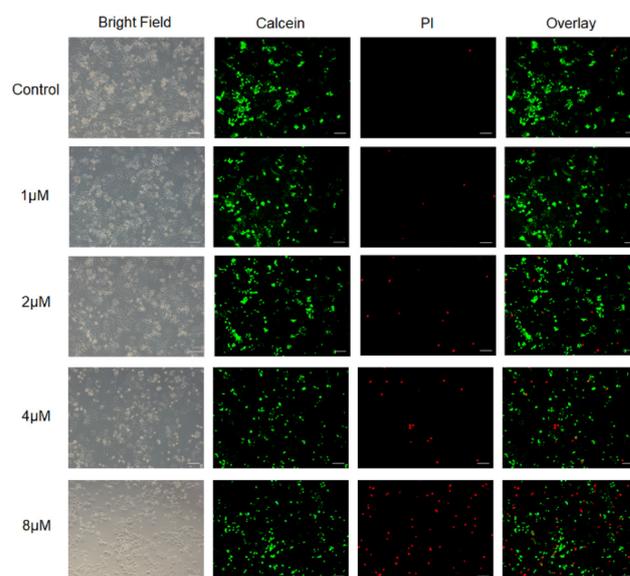

Fig. 6 Fluorescence images of Calcein-AM and PI co-stained **6**-treated NCI-H460 cells (the scale bar is 100 mm).
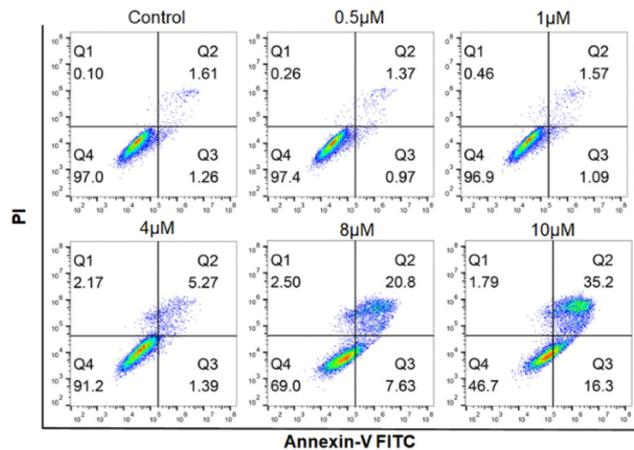
Fig. 7 Apoptosis detection in NCI-H460 cells using AnnexinV-FITC/PI double staining after 24 h treatment with various concentrations of **6**.

rescence.[20] The microscopy images (Fig. 8A) showed an apparent dose-dependent increase in green fluorescence. Compared to the control group, the mean fluorescence intensity of NCI-H460 cells incubated with 10 μM **6** increased by *ca.* 3 fold (Fig. 8B). These results indicated that **6** could induce ROS elevation.

Mitochondrial membrane potential detection

The reduced mitochondrial membrane potential (MMP) is a sign of early cell apoptosis.[21,22] To investigate the effect of complex **6** on cell MMP, we carried out flow cytometry to analyze **6**-treated NCI-H460 cells using a mitochondria fluo-
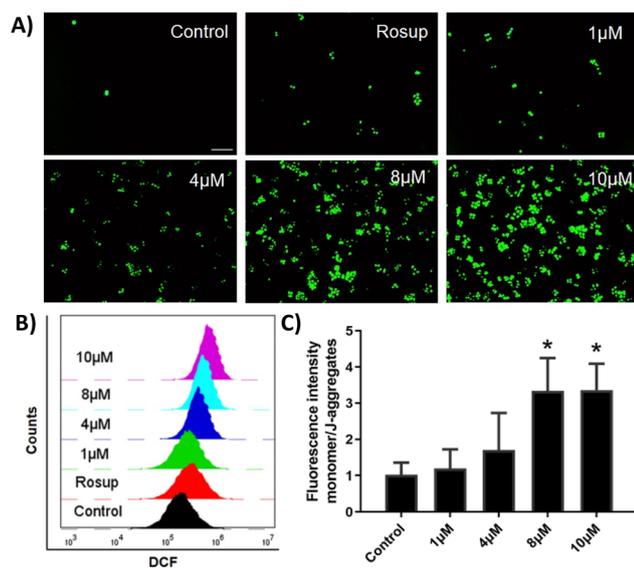

Fig. 8 Analysis of cellular ROS levels in NCI-H460 cells treated with compound **6** (1, 4, 8, and 10 μM) for 6 h and stained with DCFH-DA. Rosup was used as a positive control. (A) Cells were measured by flow cytometry. (B) Fluorescence microscopy images of cells, scale bar: 100 μm. (C) MMP analysis by flow cytometry. Cells were treated for 24 h and then stained with JC-1.

rescence probe, JC-1 (5,5′,6,6′-tetrachloro-1,1′,3,3′-tetraethyl-imidacarbocyanine iodide). JC-1 forms J-aggregates with red fluorescence at high MMP. In contrast, it exists as a J-monomer and displays green fluorescence at low MMP. Complex **6** resulted in a dose-dependent increase in the green/red fluorescence intensity ratio. Compared to the control group (1.02), the ratio was increased to 3.34 (8 μM) and 3.36 (10 μM) (*$P < 0.05$), suggesting that **6** could induce mitochondrial dysfunction, particularly the loss of MMP (Fig. 8C).

Western blot analysis of the apoptosis pathway

Cell apoptosis is known to undergo an extrinsic death receptor or intrinsic mitochondrial and endoplasmic reticulum (ER) pathway.[23–25] The caspase and Bcl-2 family proteins play essential roles in apoptosis. For example, the activation of Caspase 3 by Caspases-8 and -9 is one of the best-recognized signs of apoptosis. The Bcl-2 family acts as the regulator, which involves pro-apoptosis (Bax or Bad) and anti-apoptosis proteins (Bcl-2 or Bcl-xl).[26,27] We detected the expression of apoptosis-relevant proteins in **6**-treated NCI-H460 cells by western blotting (Fig. 9). We found that the Cleaved-Caspase 9 was activated to increase in a dose- and time-dependent manner. In addition, the downregulation of Bcl-2 and the up-regulation of Bax and Cleaved-Caspase 3 were detected in **6**-treated NCI-H460 cells (Fig. 9 and S12†). Therefore, we concluded that complex **6** could induce caspase-mediated apoptosis in NCI-H460 cells *via* the intrinsic mitochondrial pathway.

DNA damage and repair mechanisms are related to cell apoptosis.[28] H2A.X, a member of the histone H2A family, is involved in checkpoint-mediated cell cycle arrest and DNA damage repair. When cell DNA double bonds are broken, H2A.X can be phosphorylated to phospho-H2A.X (γ-H2A.X), so γ-H2A.X is regarded as a double-strand DNA-broken biomarker. PARP (poly ADP-ribose polymerase) is a DNA repair enzyme, which can be activated to be Cleaved-PARP (Cl-PARP) by recognizing damaged DNA fragments. Cleavage of PARP is an important indicator of apoptosis.[29,30] The expression level of Cl-PARP and γ-H2A.X in **6**-treated NCI-H460 cells was detected by western blotting. **6** induced time-and concen-
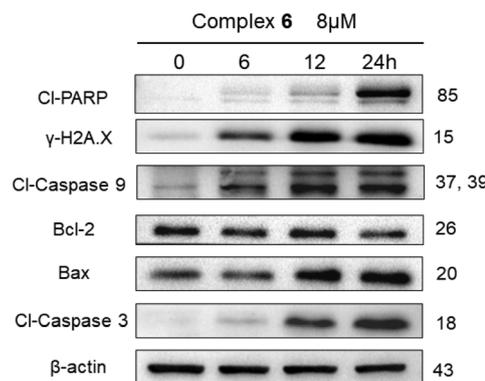

Fig. 9 Western blot analysis of DNA damage and apoptosis-related proteins in **6**-treated NCI-H460 cells at various time intervals.
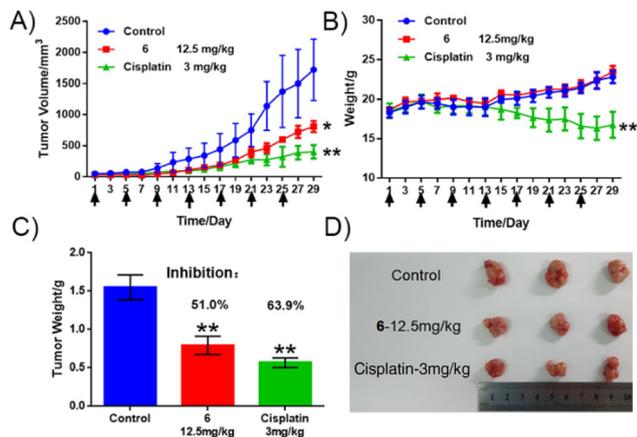
Fig. 10 *In vivo* anticancer activity of **6** in mice bearing the NCI-H460 tumor xenograft. (A) Effect of **6**, cisplatin, and the vehicle control on the tumor volume. Tumor growth was tracked using the mean tumor volume (mm^3) $\pm$ SD (n = 3). (B) Effect of **6**, cisplatin, and the vehicle control on the body weight. (C) The final tumor weight with values reported as means $\pm$ S.D. (n = 3). (*P < 0.05, **P < 0.01 represent significant difference compared with the vehicle control). (D) Photographs of tumors from the sacrificed mice at the end of the experiment.

tration-dependent up-regulation of their expression levels (Fig. 9 and S12†). Furthermore, it indicated that **6** could cause DNA damage in NCI-H460 cells, which is compatible with the result of the EdU incorporation assay.

In vivo anti-tumor activity

To evaluate the *in vivo* antitumor efficacy of **6**, we have applied an NCI-H460-bearing nude mouse tumor xenograft model. The mice were randomly divided into three groups and treated with the vehicle, complex **6** (12.5 mg kg^{-1} of mice), and cisplatin (3 mg kg^{-1} of mice) every 4 d *via* intravenous tail injection. The therapeutic effect was monitored by measuring mice's tumor volumes and body weights every 2 d (Fig. 10A and B). Remarkably, the tumor growth of the treated groups (red line for complex **6** and green line for cisplatin) was significantly inhibited compared to the control group (blue line). At the end of the experiment, the tumor sizes were determined from the sacrificed mice. Consistent with the real-time measurement, the tumor weight of the treated groups (complex **6** and cisplatin) was much lower than that of the control group (Fig. 10C). Complex **6** possessed anti-tumoral activity with an inhibitory rate of 51.0%, which is only slightly lower than 63.9% for cisplatin (*P < 0.05 **P < 0.01) (Fig. 10D). Weight loss in patients is one of the common side effects of cisplatin. In this animal test, the mice from the cisplatin-treated group resulted in steady weight loss after day 13. In contrast, the **6**-treated group exhibited unobvious weight loss throughout the experiment.

Conclusions

In summary, a series of *cis*-bis(amidine)ruthenium(III) complexes bearing two bidentate acetylacetonato(1−) ligands **1–6**

have been prepared and characterized, including X-ray analysis. All complexes show promising cytotoxicity against the tested cancer cell lines, including the cisplatin-resistance A549/DDP cell line. The representative complex **6** can inhibit colony formation and induce cell cycle arrest. It works as a cytostatic and induces cell apoptosis through the caspase-mediated mitochondrial pathway. In addition, **6** also increases intracellular ROS levels, decreases MMP, and causes DNA damage *in vitro*. *In vivo*, complex **6** shows promising antitumor efficacy with no body weight loss in nude mice. In combination with the work done by Zhu *et al.*, we demonstrated that both the *cis* and *trans* configurations of bis(amidine)ruthenium(III) complexes are promising alternatives as anticancer agents.

Materials and methods

Materials

Cisplatin (CDDP) and 3-(4,5-dimethylthiazol-2-yl)-2,5-diphenyl-tetrazoliumbromide (MTT) were purchased from Alfa. Cell Cycle Analysis Kit, ROS Assay Kit, BCA protein assay kit, MMP assay kit with JC-1, Calcein AM/PI Cell Viability/Cytotoxicity Assay Kit, and EdU Cell Proliferation Kit were obtained from Beyotime Biotechnology (Shanghai, China). FITC Annexin V Apoptosis Detection Kit I was purchased from BD Pharmingen™. The primary antibodies β-actin, GAPDH, p27, p16, CDK4, CDK2, E2F-1, p-Rb, CyclinD1, CyclinE1, Phospho-Histone H2A.X, Bax, and Bcl-2 were afforded by Cell Signaling Technology (Beverly, MA, USA). Cleaved PARP, Cleaved Caspase-3, and -9 were obtained from Abcam.

Instrumentation

Elemental analysis was performed on a Vario EL cube CHNs analyzer (Elementar, Germany). A Matrix-Assisted Laser Desorption/Ionization Time-of-Flight Mass spectrometer (Bruker, Germany) was used. UV-vis spectra were recorded on the Shimadzu UV2450-2550 spectrophotometer. Cell morphology and fluorescence imaging were observed using a ZEISS Axio Observer A1 inverted fluorescence microscope.

Synthesis. General procedure for synthesizing ruthenium(III) bis(amidine) complexes

An appropriate primary amine (2.1 mmol) was added to a solution of $[Ru^{III}(acac)_2(NCCH_3)_2]^{2+}$ (0.21 mmol) in CH_3CN (50 mL), and the mixture was stirred for 5 h at room temperature. After the removal of the volatiles, the red solid was washed with Et_2O and recrystallized from CH_3CN/Et_2O at room temperature.

cis-{Ru^{III}(acac)$_2$[NH(CH$_3$)NH(CH$_2$)$_3$(CH$_3$)$_2$](ClO$_4$)} **[1](ClO$_4$)**. Yield (85%). Anal. calcd for $C_{22}H_{42}ClN_4O_8Ru$: C, 42.14; H, 6.75; N, 8.93; found: C, 42.33; H, 6.93; N, 8.65. MALDI-TOF MS: (M$^+$) 528.

cis-{Ru^{III}(acac)$_2$[NH(CH$_3$)NH(CH$_2$)$_5$(CH$_3$)$_2$](ClO$_4$)} **[2](ClO$_4$)**. Yield (87%). Anal. calcd for $C_{26}H_{50}ClN_4O_8Ru$: C, 45.71; H, 7.38;

N, 8.20; found: C, 45.57; H, 7.09; N, 7.91. MALDI-TOF MS: (M$^+$) 584.

cis-{Ru^{III}(acac)$_2$[NH(CH$_3$)NH(CH$_2$)$_9$(CH$_3$)$_2$](ClO$_4$)} [3](ClO$_4$). Yield (82%). Anal. calcd for C$_{34}$H$_{66}$ClN$_4$O$_8$Ru: C, 51.34; H, 8.36; N, 7.04; found: C, 51.04; H, 8.66; N, 7.16. MALDI-TOF MS: (M$^+$) 696.

cis-{Ru^{III}(acac)$_2$[NH(CH$_3$)NH(CH$_2$)$_{11}$(CH$_3$)$_2$](ClO$_4$)} [4](ClO$_4$). Yield (80%). Anal. calcd for C$_{38}$H$_{74}$ClN$_4$O$_8$Ru: C, 53.60; H, 8.76; N, 6.58; found: C, 53.63; H, 8.76; N, 6.38. MALDI-TOF MS: (M$^+$) 752.

cis-{Ru^{III}(acac)$_2$[NH(CH$_3$)NH(CH$_2$)$_3$(CH$_3$)$_2$](CF$_3$SO$_3$)} [5] (CF$_3$SO$_3$). Yield (81%). Anal. calcd for C$_{23}$H$_{42}$F$_3$N$_4$O$_7$RuS: C, 40.82; H, 6.26; N, 8.28; found: C, 40.70; H, 6.06; N, 8.51. MALDI-TOF MS: (M$^+$) 528.

cis-{Ru^{III}(acac)$_2$[NH(CH$_3$)NH(CH$_2$)$_5$(CH$_3$)$_2$](CF$_3$SO$_3$)} [6] (CF$_3$SO$_3$). Yield (84%). Anal. calcd for C$_{27}$H$_{50}$F$_3$N$_4$O$_7$RuS: C, 44.25; H, 6.88; N, 7.65; found: C, 44.50; H, 6.92; N, 7.54. ESI-MS: (M$^+$) 584. Single crystals suitable for X-ray analysis were obtained by slow diffusion of Et$_2$O into a CH$_3$CN solution containing [6](CF$_3$SO$_3$) under ambient conditions.

X-ray crystallography

X-ray diffraction data of [6](CF$_3$SO$_3$) were collected on a ROD, Synergy Custom system and HyPix Diffractometer (Rigaku, Japan, Cu Kα, λ = 1.54184 Å) under 100 K. Data reductions were performed on CrysAlisPro 1.171.41.123a (Rigaku Oxford Diffraction, 2022). The structure solution was performed using SHELXT and refinement with SHELXL within the OLEX2 graphical interface.[31–33] Restraints (SADI, DELU, and SIMU) were applied for the disordered part. All non-hydrogen atoms were refined first isotropically and then anisotropically. All hydrogen atoms of the ligands were placed in calculated positions with fixed isotropic thermal parameters and included in the structure factor calculations in the final stage of full-matrix least-squares refinement. CCDC no. 2223820† contains the supplementary crystallographic data for this paper.

Cell culture

Cell culture media and supplements were purchased from Gibco. Cells were cultured in Roswell Park Memorial Institute (RPMI, 1640) or Dulbecco's modified Eagle's medium (DMEM) supplemented with 10% FBS (fetal bovine serum), 1% penicillin–streptomycin, and 1% Glutamax at 37 °C, under an atmosphere of 5% CO$_2$ and 95% air.

UV-Visible spectroscopy

The solvent stability of compounds 1–6 in DMSO and PBS was investigated by UV-vis spectroscopy. The complexes were dissolved in DMSO or PBS (1% DMSO) and measured using a UV2450-2550 spectrophotometer for 24 h. The data were curved by GraphPad Prism 8 software.

Cytotoxicity MTT assay

Cells were cultured in 96-well plates at 6000 cells per well, followed by incubation at 37 °C for 24 h to allow attachment, then the addition of dilutions of the test compounds, which were dissolved in DMSO while cisplatin was dissolved in water, and incubation for 48 h. Cisplatin was introduced as a control. The compound-containing medium was replaced by fresh medium with 0.5 mg mL^{-1} MTT and incubated for 1.5 h. After incubating, DMSO was added to each well when the medium containing MTT was removed. The absorbance was measured at 570 nm using Infinite M200 (Swiss, Tecan). IC$_{50}$ values were calculated from concentration-effect curves by logarithmic interpolation using Origin 8. Each assay was carried out three times, and the results are expressed as the mean ± SEM.

Plate colony formation assay

The NCI-H460 cells were seeded in 6-well plates (1000 cells per well). After 24 h attachment, the cells were exposed to different concentrations of compound 6 for 48 h. Then, after drug washout and incubation for 7 d, the cells were fixed with 4% paraformaldehyde for 20 min and stained with 1% crystal violet solution for 30 min to observe colonies.

EdU incorporation assay

The EdU incorporation assay was performed using the EdU Cell Proliferation Kit to test DNA synthesis. NCI-H460 cells were inoculated in 12-well plates. After the cells were treated with different concentrations of complex 6 for 24 h, the cells were cultured with 20 µM EdU for 2 h. Hydroxyurea was used as a positive control. After EdU labeling of the cells, 500 µL of Click reaction solution was added to each well and incubated at room temperature for 30 min in the dark. Then, the cells were incubated with Hoechst 33342 to stain the cell nuclei. Subsequently, the stained cells were washed with PBS and observed with a ZEISS Observer A1 inverted fluorescence microscope.

Calcein AM/PI staining

The living and dead cells were detected using the Calcein AM/PI Cell Viability/Cytotoxicity Assay Kit. NCI-H460 cells were seeded in 12-well plates and treated with complex 6 for 24 h. Then the cells were washed with PBS and stained with Calcein AM/PI working solution (1000×) for 30 min in the dark at 37 °C. Finally, the cells were washed with PBS twice and observed under a ZEISS Observer A1 inverted fluorescence microscope.

Cell cycle analysis

NCI-H460 cells were seeded in 6-well plates and treated with 8 µM 6 at various time intervals. Then, the cells were collected and subsequently fixed with ice-cold 70% ethanol and kept at 4 °C for 24 h. Finally, the cells were washed with PBS, suspended in a PI solution (500 µL staining buffer, 12 µL RNase (50×) and 25 µL propidium iodide (20×), and stained for 30 minutes at 37 °C in the dark. All samples were then analyzed using a flow cytometer.

Cell apoptosis assay

NCI-H460 cells were seeded into 6-well plates. Complex 6 (0.5, 1, 4, 8, and 10 µM) was added to the cells for 24 h treatment,

or the cells were treated with 8 μM **6** for 6, 12, 24, 36, and 48 h. Then, the cells were collected, centrifuged at 1000 rpm for 5 min, washed with PBS twice, resuspended in 500 μL binding buffer (1×), and stained with 5 μL Annexin V and 5 μL propidium iodide for 10 min at room temperature. The flow cytometer was used for the analysis.

ROS detection

NCI-H460 cells were plated in 6-well plates and treated with compound **6** at the required concentrations for 6 h. Rosup (10 μM) was incubated for 20 min as a positive control. The treated cells were collected and washed with a serum-free medium three times. Then, the cells were stained with 10 μmol L^{-1} DCFH-DA for 20 min at 37 °C in the dark. At last, the fluorescence intensity was detected using a flow cytometer and ZEISS Observer A1 inverted fluorescence microscope.

MMP detection

NCI-H460 cells were cultured with complex **6** for 24 h at indicated concentrations. The treated cells were digested and collected. Then, the cells were incubated with JC-1 staining buffer for 20 min at 37 °C in the dark. The cells were washed with JC-1 washing buffer (1×) twice and analyzed by flow cytometry to detect the red/green fluorescence intensity.

Western blot analysis

NCI-H460 cells were seeded in 6-well plates. After treatment with **6** at different concentrations and times, the cells were lysed in cell lysis buffer, which contains a protease inhibitor. The protein was extracted and quantified using the BCA Protein Assay Kit. The protein samples were separated on 8–15% SDS-PAGE and transferred onto a nitrocellulose membrane (BOSTER). After blocking with 5% nonfat milk for 1 h at room temperature, the membranes were probed with the primary antibody overnight at 4 °C and incubated with a secondary antibody (anti-rabbit or anti-mouse, 1 : 10 000) for 1 h at room temperature. The target proteins were examined using a High ChemiDoc XRS (Bio-Rad ChemiDoc XRS+, USA).

In vivo xenograft model

The mice were approved by the Animal Laboratory Center at Shantou University Medical College; the license number is SYXK2022-0079 (Guangdong, China). 3×10^6 NCI-H460 cells were suspended with 0.1 mL of serum-free culture medium and injected subcutaneously into the right flank region of BALB/c-nu mice to establish the xenograft models. When the xenograft tumor volume reached about 50–100 mm^3, the mice were randomly divided into solvent control and treatment groups (n = 3 per group). Complex **6** was given *via* intravenous tail injection every 4 days at 12.5 mg kg^{-1} (10% v/v PET/PBS). PET solution = (polyethylene glycol 400, 60%; ethanol 30%; Tween 80, 10%). Cisplatin was given to mice at a dosage of 3 mg kg^{-1} and used as a positive reference for comparison. Control mice received the solvent (10% v/v PET/PBS) *via* intravenous tail injection. The tumor size and body weight were monitored every 2 d. The tumor volumes were determined

with a digital caliper by measuring the length (l) and width (w) and calculating with the formula of $V = lw^2/2$. Meanwhile, the body weight of mice was measured and taken as a parameter of systemic toxicity. On day 29, the animals were sacrificed and the tumors were weighed and recorded.

Conflicts of interest

There are no conflicts to declare.

Acknowledgements

References

1 M. G. Ferraro, M. Piccolo, G. Misso, R. Santamaria and C. Irace, Bioactivity and Development of Small Non-Platinum Metal-Based Chemotherapeutics, *Pharmaceutics*, 2022, **14**, 954–986.

2 W. Q. Huang, C. X. Wang, T. Liu, Z. X. Li, C. Pan, Y. Z. Chen, X. Lian, W. L. Man and W. X. Ni, A cytotoxic nitrido-osmium(VI) complex induces caspase-mediated apoptosis in HepG2 cancer cells, *Dalton Trans.*, 2020, **49**, 17173–17182.

3 X. Li, Y. Yu, Q. Chen, J. Lin, X. Zhu, X. Liu, L. He, T. Chen and W. He, Engineering cancer cell membrane-camouflaged metal complex for efficient targeting therapy of breast cancer, *J. Nanobiotechnol.*, 2022, **20**, 401.

4 S. Thota, D. A. Rodrigues, D. C. Crans and E. J. Barreiro, Ru (II) Compounds: Next-Generation Anticancer Metallotherapeutics?, *J. Med. Chem.*, 2018, **61**, 5805–5821.

5 Z. Zhao, X. Zhang, C. E. Li and T. Chen, Designing luminescent ruthenium prodrug for precise cancer therapy and rapid clinical diagnosis, *Biomaterials*, 2019, **192**, 579–589.

6 L. Zeng, P. Gupta, Y. Chen, E. Wang, L. Ji, H. Chao and Z. S. Chen, The development of anticancer ruthenium(II) complexes: from single molecule compounds to nanomaterials, *Chem. Soc. Rev.*, 2017, **46**, 5771–5804.

7 D. Havrylyuk, D. K. Heidary, Y. Sun, S. Parkin and E. C. Glazer, Photochemical and Photobiological Properties of Pyridyl-pyrazol(in)e-Based Ruthenium(II) Complexes with Sub-micromolar Cytotoxicity for Phototherapy, *ACS Omega*, 2020, **5**, 18894–18906.

8 D. Havrylyuk, B. S. Howerton, L. Nease, S. Parkin, D. K. Heidary and E. C. Glazer, Structure-activity relationships of anticancer ruthenium(II) complexes with substi-

tuted hydroxyquinolines, *Eur. J. Med. Chem.*, 2018, **156**, 790–799.

9 A. C. Hachey, D. Havrylyuk and E. C. Glazer, Biological activities of polypyridyl-type ligands: implications for bio-inorganic chemistry and light-activated metal complexes, *Curr. Opin. Chem. Biol.*, 2021, **61**, 191–202.

10 E. Wachter, A. Zamora, D. K. Heidary, J. Ruiz and E. C. Glazer, Geometry matters: inverse cytotoxic relationship for cis/trans-Ru(ii) polypyridyl complexes from cis/trans-$[PtCl_2(NH_3)_2]$, *Chem. Commun.*, 2016, **52**, 10121–10124.

11 C. Li, K. W. Ip, W. L. Man, D. Song, M. L. He, S. M. Yiu, T. C. Lau and G. Zhu, Cytotoxic (salen)ruthenium(iii) anti-cancer complexes exhibit different modes of cell death directed by axial ligands, *Chem. Sci.*, 2017, **8**, 6865–6870.

12 Y. Kasahara, Y. Hoshino, K. Shimizu and G. P. Satô, Reaction of tris(β-diketonato) ruthenium(iii) complexes with strong acids in acetonitrile. Formation of bis(aceto-nitrile)bis(β-diketonato)ruthenium(iii) complexes, *Chem. Lett.*, 1990, **19**, 381–384.

13 H. Z. Liu, W. Xiao, Y. P. Gu, Y. X. Tao, D. Y. Zhang, H. Du and J. H. Shang, Polysaccharide from Sepia esculenta ink and cisplatin inhibit synergistically proliferation and meta-stasis of triple-negative breast cancer MDA-MB-231 cells, *Iran. J. Basic Med. Sci.*, 2016, **19**, 1292–1298.

14 M. Malumbres and M. Barbacid, To cycle or not to cycle: a critical decision in cancer, *Nat. Rev. Cancer*, 2001, **1**, 222–231.

15 V. Ramu, M. R. Gill, P. J. Jarman, D. Turton, J. A. Thomas, A. Das and C. Smythe, A Cytostatic Ruthenium(ii)-Platinum (ii) Bis(terpyridyl) Anticancer Complex That Blocks Entry into S Phase by Up-regulating p27(KIP1), *Chemistry*, 2015, **21**, 9185–9197.

16 R. Roskoski Jr., Cyclin-dependent protein serine/threonine kinase inhibitors as anticancer drugs, *Pharmacol. Res.*, 2019, **139**, 471–488.

17 M. Palaiologou, J. Koskinas, M. Karanikolas, E. Fatourou and D. G. Tiniakos, E2F-1 is overexpressed and pro-apopto-tic in human hepatocellular carcinoma, *Virchows Arch.*, 2012, **460**, 439–446.

18 C. Gorrini, I. S. Harris and T. W. Mak, Modulation of oxidative stress as an anticancer strategy, *Nat. Rev. Drug Discovery*, 2013, **12**, 931–947.

19 M. Ye, W. Q. Huang, Z. X. Li, C. X. Wang, T. Liu, Y. Chen, C. H. Hor, W. L. Man and W. X. Ni, Osmium(vi) nitride triggers mitochondria-induced oncosis and apoptosis, *Chem. Commun.*, 2022, **58**, 2468–2471.

20 M. J. Reiniers, L. R. de Haan, L. F. Reeskamp, M. Broekgaarden, R. F. van Golen and M. Heger, Analysis and Optimization of Conditions for the Use of 2′,7′-Dichlorofluorescein Diacetate in Cultured Hepatocytes, *Antioxidants*, 2021, **10**, 674–691.

21 A. V. Gyulkhandanyan, D. J. Allen, S. Mykhaylov, E. Lyubimov, H. Ni, J. Freedman and V. Leytin, Mitochondrial Inner Membrane Depolarization as a Marker of Platelet Apoptosis : Disclosure of Nonapoptotic Membrane Depolarization, *Clin. Appl. Thromb./Hemostasis*, 2017, **23**, 139–147.

22 D. Wan, B. Tang, Y. J. Wang, B. H. Guo, H. Yin, Q. Y. Yi and Y. J. Liu, Synthesis and anticancer properties of ruthenium(ii) complexes as potent apoptosis inducers through mitochon-drial disruption, *Eur. J. Med. Chem.*, 2017, **139**, 180–190.

23 H. Wang, H. Liu, Z. M. Zheng, K. B. Zhang, T. P. Wang, S. S. Sribastav, W. S. Liu and T. Liu, Role of death receptor, mitochondrial and endoplasmic reticulum pathways in different stages of degenerative human lumbar disc, *Apoptosis*, 2011, **16**, 990–1003.

24 D. R. Green and F. Llambi, Cell Death Signaling, *Cold Spring Harbor Perspect. Biol.*, 2015, **7**, 12–36.

25 B. A. Carneiro and W. S. El-Deiry, Targeting apoptosis in cancer therapy, *Nat. Rev. Clin Oncol.*, 2020, **17**, 395–417.

26 N. A. Thornberry and Y. Lazebnik, Caspases: enemies within, *Science*, 1998, **281**, 1312–1316.

27 R. Singh, A. Letai and K. Sarosiek, Regulation of apoptosis in health and disease: the balancing act of BCL-2 family proteins, *Nat. Rev. Mol. Cell Biol.*, 2019, **20**, 175–193.

28 B. B. Zhou and S. J. Elledge, The DNA damage response: putting checkpoints in perspective, *Nature*, 2000, **408**, 433–439.

29 E. P. Rogakou, D. R. Pilch, A. H. Orr, V. S. Ivanova and W. M. Bonner, DNA double-stranded breaks induce histone H2AX phosphorylation on serine 139, *J. Biol. Chem.*, 1998, **273**, 5858–5868.

30 J. C. Ame, C. Spenlehauer and G. de Murcia, The PARP superfamily, *Bioessays*, 2004, **26**, 882–893.

31 G. M. Sheldrick, SHELXT - integrated space-group and crystal-structure determination, *Acta Crystallogr., Sect. A: Found. Adv.*, 2015, **71**, 3–8.

32 G. M. Sheldrick, Crystal structure refinement with SHELXL, *Acta Crystallogr., Sect. C: Struct. Chem.*, 2015, **71**, 3–8.

33 R. J. Gildea, L. J. Bourhis, O. V. Dolomanov, R. W. Grosse-Kunstleve, H. Puschmann, P. D. Adams and J. A. Howard, iotbx.cif: a comprehensive CIF toolbox, *J. Appl. Crystallogr.*, 2011, **44**, 1259–1263.